

# Combined Experimental and First Principles Study on Nanostructured NbFeSb Half-Heusler Alloy Synthesized by Mechanical Alloying

Cleverton Oliveira Dias<sup>a</sup>, Joziano Rony de Miranda Monteiro<sup>a</sup> , Leonardo Soares de Oliveira<sup>b</sup>,  
Puspitapallab Chaudhuri<sup>a</sup>, Sérgio Michielon de Souza<sup>a</sup>, Daniela Menegon Trichês<sup>a\*</sup> 

<sup>a</sup>Universidade Federal do Amazonas, Departamento de Física, 69077-000, Manaus, AM, Brasil.

<sup>b</sup>Technical University of Denmark, Department of Physics, 2800, Lyngby, Kgs, Denmark.

Received: June 26, 2022; Revised: November 01, 2022; Accepted: December 12, 2022

The Half-Heusler semiconductor alloys can be used efficiently as thermoelectric materials to transform the waste heat into useful electrical energy. The low-cost and large-scale production of suitable half-Heusler alloys are important in the present context. In this work, a nanostructured half-Heusler NbFeSb alloy is obtained by mechanical alloying with 15h of milling. The structural parameters of the sample are investigated by powder X-ray diffraction followed by Rietveld refinement. Differential scanning calorimetry indicates that the NbFeSb phase is stable up to about 420 K. The electrical resistivity is obtained as a function of temperature. A band gap of 0.37(3) eV is obtained from UV-Vis measurements. Density functional theory calculation shows an indirect band gap of 0.52 eV. Analyses of the obtained data indicate that structural defects and nanometric crystallites sizes present in the nanostructured NbFeSb produced by mechanical alloying do not degrade the electrical and optical properties of the compound.

**Keywords:** Nanostructured alloys, thermoelectric materials, half-heusler alloys, mechanical alloying, density functional theory.

## 1. Introduction

Over the last few decades, Half-Heusler (HH) alloys have been drawing much attention of the material science community worldwide, both experimental and theoretical, for their potential utilities in sustainable energy related applications<sup>1-16</sup>. They are among the most promising thermoelectric materials that can be used at medium to high temperature power generation purposes<sup>9</sup>. Additionally, the excellent mechanical and thermal stability and low toxicity of these compounds make them suitable for industrial and commercial usage in the field of environment friendly clean energy production<sup>9,10</sup>.

Typically, the HH alloys are intermetallic semiconductors having the general formula of XYZ, where X, Y are transition metals or rare-earth metals, with X being more electropositive than Y and Z is a main group element. They crystallize in the cubic Mg-Ag-As-type structure (space group F-43m) forming three filled interpenetrating face-centered-cubic (fcc) sublattices and one vacant fcc sublattice<sup>1</sup>.

The thermoelectric efficiency of a given material is determined by the dimensionless figure of merit (ZT) which defined in terms of the Seebeck coefficient ( $S$ ), the electrical conductivity ( $\sigma$ ), the thermal conductivity ( $k$ ) as  $ZT = S^2\sigma T / k$ , where  $T$  is the absolute working temperature. The higher the ZT-value, the better is the efficiency of thermoelectric conversion. In order to obtain a high value of ZT, it is essential that the material possesses either a high power factor ( $S^2\sigma$ ) or a low thermal conductivity. However,

these three physical parameters are interdependent and this makes it challenging to synthesize high-ZT thermoelectric materials with individual control over the parameters. In recent years, a successful strategy that is being used to decrease thermal conductivity without adversely affecting the other properties in various thermoelectric materials is nanostructuring and/or doping<sup>1,4,9,10,14,17-19</sup>.

The technique of Mechanical Alloying (MA) has been used extensively to synthesize high-entropy alloys, amorphous alloys, supersaturated solid solutions and nanostructured materials<sup>20</sup>. The advantages of MA include low temperature processing, composition control, low-cost equipment, and the possibility of scaling up. On the other hand, the disadvantages include the possibility of powder contamination during milling and the difficulty in successful consolidation of MA powders<sup>20</sup>.

Among the HH alloys, NbFeSb has attracted more attention due to its excellent thermoelectric performances at high temperatures<sup>3</sup>. Moreover, the HH NbFeSb alloy enjoys the advantages of being non-expensive, abundant, and non-toxic<sup>16</sup>. Mostly, NbFeSb has been synthesized by conventional arc-melting followed by long heat treatments at relatively high temperatures<sup>2,4,12,13</sup>. Recently, it has been suggested that MA can be a simple and viable technique to synthesize NbFeSb single phase HH alloy<sup>8,21</sup>. Although these works perform consolidation of the milled powders via spark plasma sintering, we were motivated by them. Therefore, we have synthesized a nanostructured NbFeSb HH alloy only by MA, without any other processing. The structural

\*e-mail: triches@ufam.edu.br

parameters of the milled NbFeSb sample have been investigated by powder X-ray Diffraction (XRD) followed by Rietveld refinement. The thermal stability and the electrical conductivity of the sample have been analyzed by differential scanning calorimetry (DSC) and complex impedance spectroscopy (CIS), respectively. The electronic properties have been investigated by UV-Vis measurements and density functional theory (DFT) calculations.

## 2. Materials and Methods

### 2.1. Sample preparation and measurement techniques

A mixture of high-purity (99,7%) powdered elemental Nb (Alfa Aesar), Fe (ASC) and Sb (Alfa Aesar) with a stoichiometry of 1:1:1 was sealed under argon atmosphere into a cylindrical steel vial along with several steel balls, with 5:1 ball-to powder ratio (BPR). MA was performed for 25h at room temperature in a high-energy ball-mill (Spex Mixer/Mill 8000). The milling process was paused five times during the milling period in order to follow de-structural evolution of the powdered sample by XRD measurements.

The XRD measurements were performed in the angular range of  $10^\circ$  to  $100^\circ$  ( $2\theta$ ), with step sizes of  $0.01313^\circ$ , with an interval of 60s per step using an Empyrean Analytical diffractometer operating in reflection mode and x-ray source of  $\text{CuK}_\alpha$  radiation ( $\lambda = 1.5418 \text{ \AA}$ ). The diffractometer was equipped with Bragg-Brentano HD mirror,  $0.02$  rad soller slit,  $1^\circ$  anti-scattering slit and  $1/4^\circ$  divergence slit in the incident beam, and a  $0.04$  rad soller slit and a  $9$  mm anti-scattering slit for the diffracted beam. The instrument was operated at  $40\text{kV}$  of accelerating voltage and  $40$  mA of applied current. The X-ray photons were identified utilizing a PIXcel3D-Medipix3  $1 \times 1$  area detector. In situ high temperature XRD measurements were performed from  $300$  K to  $420$  K with a heating rate of  $10$  K/min using an Anton Paar TTK 450 chamber coupled to Empyrean Analytical diffractometer.

The DSC measurement of 25h milled sample was performed in the range of  $293$  to  $873$  K on a TA Instruments SDT Q600 thermoanalyzer, with a heating rate of  $10$  K/min under a continuous nitrogen gas flow of  $30$  ml/min.

The CIS measurements were performed using a Solartron 1260 frequency response analyzer as a function of frequency ( $1\text{Hz}$ – $1$  MHz) in the temperature range of  $3$  K to  $390$  K. For this measurement, the 25h MA powder was cold pressed in a pellet with an area of  $1.8$  mm<sup>2</sup> and thickness of  $2.5$  mm. The amplitude of the applied alternating electric field was  $0.5$  V/mm.

The crystalline powders were diluted in water followed by simple/ordinary filtration using a  $0.22$   $\mu\text{m}$  diameter filter paper. A small quantity was put in a quartz cuvette in order to measure the absorbance  $\text{Abs}(\lambda)$  in the wavelength range of  $200$  -  $1000$  nm. Absorbance measurements were performed on a UV-Vis spectrophotometer (Global Trade Technology, Brazil). The bandgap energy value was obtained by a Tauc plot<sup>22</sup>.

### 2.2. Theory and calculation

The XRD pattern was refined by using Rietveld method as implemented in the GSAS software package<sup>23</sup> following

the recommendations of the IUCr<sup>24</sup>. The fourth-order Chebyshev polynomials were used to fit the inelastic scattering background. As for the peak profile analysis, a modified Thompson-Cox-Hasting pseudo-Voigt profile function (CW profile function 4 in the GSAS package) was used. The instrumental broadening was analyzed by a certified LaB6 standard (NIST 660b) and the obtained values of  $U = 0.0$ ,  $V = -0.0036$  and  $W = 0.0023$  remained unaltered. The texture effects were considered by using the spherical harmonics preferential orientation model<sup>25</sup>.

The XRD line broadening effects due to small domain sizes and microstrains can be assessed assuming that the Lorentzian component of the structurally broadened profile is due to the small crystallite size, and the Gaussian component of the structurally broadened profile is due to microstrain. The apparent crystallite size or domain size  $D$  is given by Scherrer's equation<sup>26</sup>

$$D_{hkl} = \frac{K\lambda}{\beta_L \cos\theta_{hkl}} \quad (1)$$

and microstrain  $\epsilon$  by

$$\epsilon_{hkl} = \frac{\beta_G}{4\tan\theta_{hkl}} \quad (2)$$

for each  $hkl$  peak. In Equations (1) and (2),  $K$  is the Scherrer constant<sup>27</sup>,  $\lambda$  is the incident wavelength,  $\beta_L$  and  $\beta_G$  are the Lorentzian and Gaussian integral breadths respectively. The integral breadths can be expressed in terms of the full width at half maximum (FWHM) and mixture coefficient  $\eta$  parameter, obtained directly from the Rietveld analysis as:

$$\beta_G = \frac{\text{FWHM}}{2} \sqrt{\frac{\pi(1 - 0.74417\eta - 0.24781\eta^2 - 0.00810\eta^3)}{\ln 2}} \quad (3)$$

and

$$\beta_L = \frac{\pi \text{FWHM}}{2} (0.72928\eta + 0.19289\eta^2 + 0.07783\eta^3) \quad (4)$$

All Rietveld structural refinements of this work achieved well convergence factor considering  $\eta = 0.75$ .

In the Williamson-Hall method the total integral breadth  $\beta$  can be considered as  $\beta = \beta_L + \beta_G$  of Equations (1) and (2) leading to a linear equation as follows:

$$\beta \cos\theta = \frac{K}{D} + 4\epsilon \sin\theta \quad (5)$$

Considering an isotropic microstructure such as the present sample, this equation should approximately fit the experimental data. The mean crystallites size ( $D$ ) and the microstrain ( $\epsilon$ ) can be calculated from its linear coefficient and the slope, respectively.

The energy bands and density of states (DOS) were obtained by DFT methods as implemented in Quantum Espresso package<sup>28</sup>. The exchange correlation energy was described by Perdew-Burke-Ernzerhof (PBE) functional<sup>29</sup> based on the generalized gradient approximation (GGA). For the constraint-free geometry optimization of the NbFeSb unit

cell the Broyden–Fletcher–Goldfarb–Shanno (BFGS) quasi Newton algorithm was adopted with the convergence thresholds set at  $10^{-4}$  eV/Å for force and  $10^{-6}$  eV for energy. The kinetic energy cutoff for the wave functions and charge density were taken as 80 Ry and 480 Ry, respectively. The Brillouin zone of the supercell was sampled by  $6 \times 6 \times 6$  Monkhorst-Pack k-point grid<sup>30</sup>. The structural models were plotted using the XCrySDen package<sup>31</sup>. The energy gap was calculated for the above unit cell and compared with the experimental value.

### 3. Results and Discussion

#### 3.1. Structural and thermal characterization

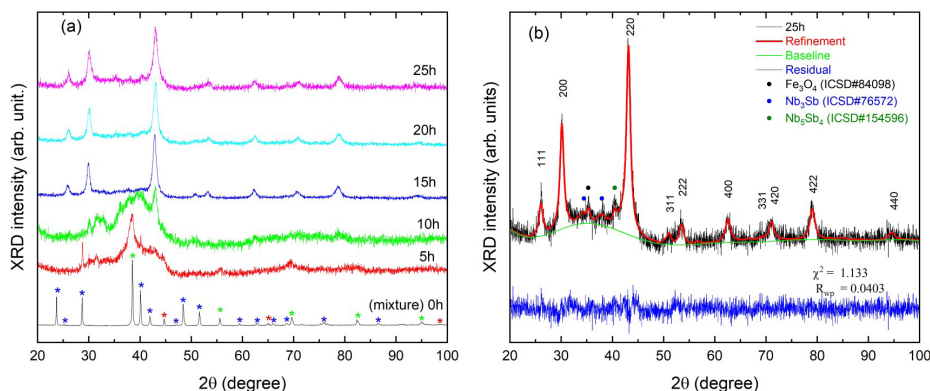
Figure 1a depicts the XRD measurements of the prepared NbFeSb sample as a function of the milling time. The XRD peaks of the precursor mixture (0 h) are identified as Nb (ICSD#760011, marked by green asterisks), Fe (ICSD#64998, marked by red asterisks) and Sb (ICSD#53795, marked by blue asterisks)<sup>32</sup>. After 5 h of milling, the peaks related to the precursors are enlarged indicating severe deformation. After 10 h, the diffraction peaks of precursors almost disappear indicating that the sample has acquired a critical size (nanocluster) or suffered a transition to an amorphous phase. On the other hand, a new peak emerges in the XRD pattern around 43 degrees. This new peak has been identified as cubic NbFeSb (space group F-43m, n°. 216, ICSD#83928). After 15 h, one can observe the complete nucleation of HH NbFeSb. The large increase in the intensity of the peak indicates that the size of the crystallites is of nanometric scale. For longer milling times ranging from 15 to 25 h, no appreciable changes in the evolution of the diffractograms are observed. Thus, with only 15h of milling, a stable NbFeSb alloy is formed. Further analyses have been performed on the 25h milled sample.

Figure 1b presents the detailed XRD pattern of the sample, after 25 h of milling at room temperature and the result of Rietveld refinement. The phase content obtained in the refinement is 73.5 wt% of NbFeSb, 10.1 wt% of  $\text{Fe}_3\text{O}_4$ , 9.7 wt% of  $\text{Nb}_3\text{Sb}$  and 6.7 wt% of  $\text{Nb}_5\text{Sb}_4$ . The refined lattice parameters of the HH NbFeSb are  $a = b = c = 5.944(2)$  Å and the cell volume is  $204.4(1)$  Å<sup>3</sup>. The goodness-of-fit

parameters<sup>33</sup> are  $R_{wp} = 4.03\%$  and  $\chi^2 = 1.133$ . The region between  $30^\circ$  and  $40^\circ$  presents an elevation due to the presence of an amorphous phase. In this region it is also possible to observe the diffraction peaks associated with the  $\text{Fe}_3\text{O}_4$  (ICSD#84098, marked by black sphere),  $\text{Nb}_3\text{Sb}$  (ICSD#76572, marked by blue spheres) and  $\text{Nb}_5\text{Sb}_4$  (ICSD#154596, marked by green sphere) phases. It should be noted that the MA process has been repeated to ensure the reproducibility, and the same phases have been obtained. Besides this, Pedersen et al.<sup>21</sup> also observed secondary phases in the mechanically alloyed NbFeSb in this same region. Figure 1b also shows the Miller indices of the cubic HH NbFeSb phase.

The NbFeSb peaks in the experimental XRD pattern shown in Figure 1b are broadened, indicating that the crystallites sizes are very small. The mean size of the crystallites can be estimated from the refined XRD pattern taking into account the line broadening caused by both crystallite size and lattice microstrain through Equation 5. Figure 2 shows the graphical linearization of Equation 5, i.e., the plot  $\hat{a}\cos\theta$  versus  $4\sin\theta$ . In this figure, it is observed that the total integral breadth ( $\beta$ ) of the NbFeSb diffraction peaks increase monotonically with the angle  $\theta$ , indicating that the sample exhibits homogeneous distribution of crystallite size and microstrain. Thus, it is possible to make a linear adjustment to Equation 5 (Williamson-Hall) and obtain the lattice microstrain value from the slope,  $\varepsilon = 0.083\%$ , and the mean crystallite size from the intercept with the axis,  $D = 9.54(2)$  nm.

Figure 3a shows the DSC curve of the 25h milled sample. The curve displays an enlarged exothermic peak with two main shoulders - one at around 540 K and another at around 630 K. Exothermic behavior in DSC measurements is associated with the release of tensions in the lattice, crystallization of amorphous phases, oxidation. The sample recovered after the DSC measurement was analyzed by XRD (Figure 3b) and it presented diffraction peaks of the  $\text{Fe}_2\text{O}_3$  (ICSD#33643),  $\text{FeNbO}_2$  (ICSD#47187),  $\text{NbO}_2$  (ICSD#75198) and Sb (ICSD#53795). The  $\text{Fe}_2\text{O}_3$  phase was already present in the sample, as shown in Figure 1b. The  $\text{FeNbO}_2$  and  $\text{NbO}_2$  oxides may be also present in form of nanoclusters, undetectable by XRD diffraction. So, the exothermic behavior in DSC



**Figure 1.** a) XRD patterns of NbFeSb synthesis for different milling times. b) XRD pattern of the NbFeSb and the Rietveld refinement. The Miller indices of NbFeSb phase are indicated.

measurement (Figure 3a) may be associated with the growth of the oxides at expense of NbFeSb phase and the release of tensions in the lattice of these oxides.

In order to check the thermal stability of the NbFeSb alloy, we have performed in situ high temperature XRD measurements with temperature varying from 300K up to 420 K. The results are depicted in Figure 3c and no structural changes are observed. Therefore, we can conclude that the NbFeSb alloy produced by MA is stable up to 420 K, as shown in Figure 3c. However, the XDR measurement of the sample that was heated and cooled after DSC measurement (Figure 3b), shows that the NbFeSb phase no longer exists,

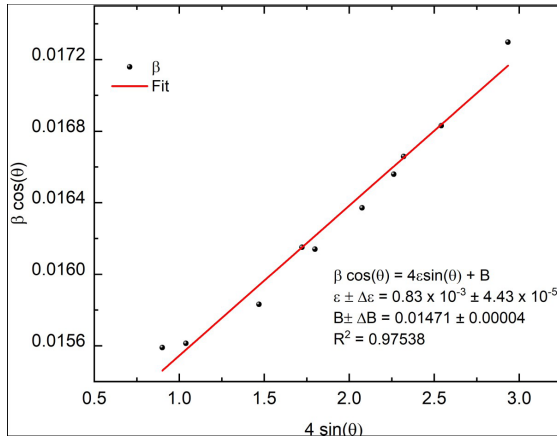


**Figure 2.** Linear adjustment of  $\beta$  to Equation 5 (Williamson-Hall).

and the phases present in the sample are  $\text{Fe}_2\text{O}_3$ ,  $\text{NbFeO}_2$ , Sb and  $\text{NbO}_2$ . Thus, we conclude that the NbFeSb alloy produced by MA gets completely decomposed between 420 K and 800 K. Thereby, in order to verify the thermal stability, it is important always to perform thermal analysis on NbFeSb alloys produced by MA. This is a very important observation, since other studies about this compound obtained by MA<sup>8,21</sup> do not perform thermal analysis in the mechanically alloyed sample.

### 3.2. Complex impedance spectroscopy (CIS)

Figure 4a presents the impedance spectrum of the 25h sample, obtained at room temperature. The feature of the curve between 1 Hz and 1 KHz, as displayed by the sample, suggests a circuit in which a resistor with resistance R is connected directly to the battery<sup>34</sup>. In this case, the complex impedance will be  $Z^* = \text{Re}[Z^*]$ , so that  $\text{Re}[Z^*] = R$  and  $\text{Im}[Z^*] = 0$ . The impedance spectrum characterizes the sample to have a purely resistive behavior with approximately constant resistance of 3.3  $\Omega$ . No significant variation of the resistance is observed in the frequency range of 1Hz – 1MHz.

The imaginary impedance has an increasing variation for frequencies greater than 1 kHz. Physically this increase can be caused by the charge accumulation at the limits of the grain boundaries. The sample has nanometric crystallites sizes, as show in Section 3.1 ( $D = 9.54(2)$  nm) and, therefore, it possesses a large amount of grain boundaries where the charges accumulate, generating greater lag between the voltage and electric current<sup>35</sup>.

Figure 4b displays the electrical resistivity ( $\rho$ ) plotted as a function of temperature ( $T$ ) for the 25h milled sample.

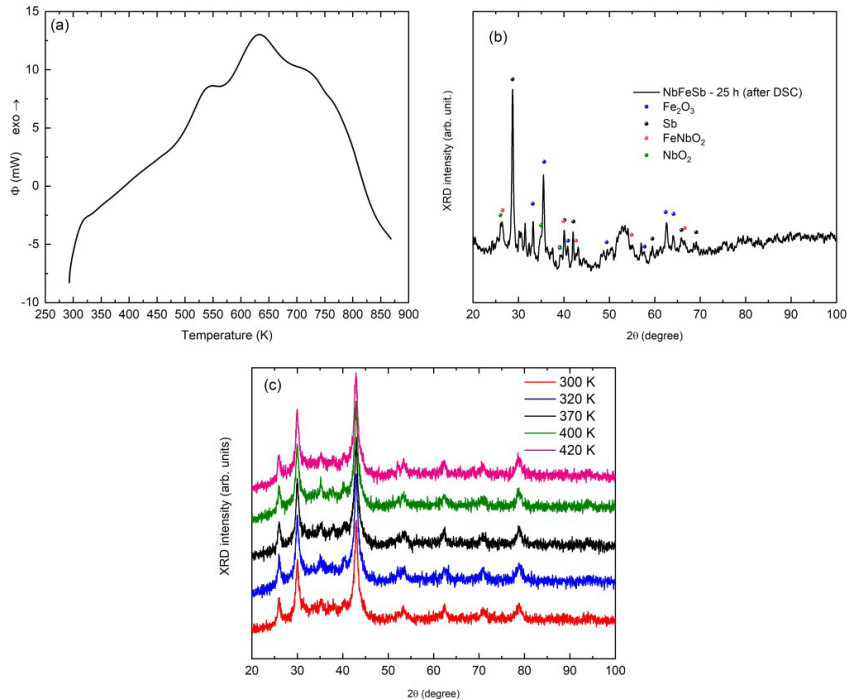


**Figure 3.** a) DSC curve of the 25h milled sample. (b) XRD measurement of the sample recovered after the DSC measurement. (c) In situ high temperature XRD measurements of the 25h milled sample.

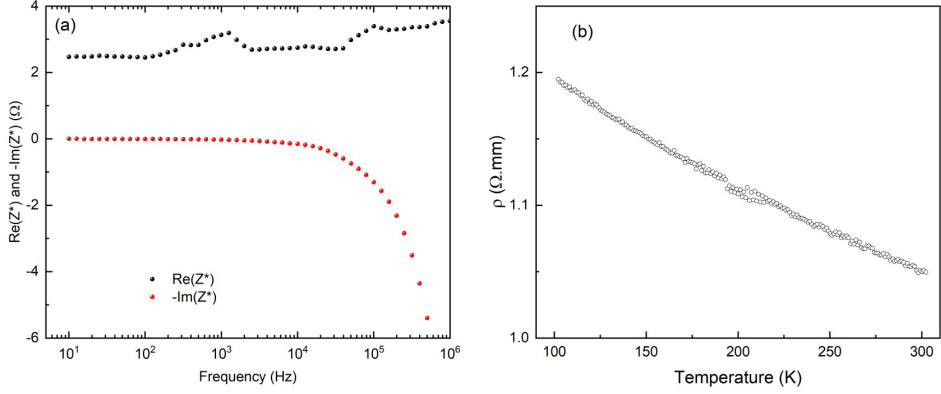


**Figure 4.** a) Impedance spectrum at room temperature and b) resistivity as a function of temperature for the 25h sample.

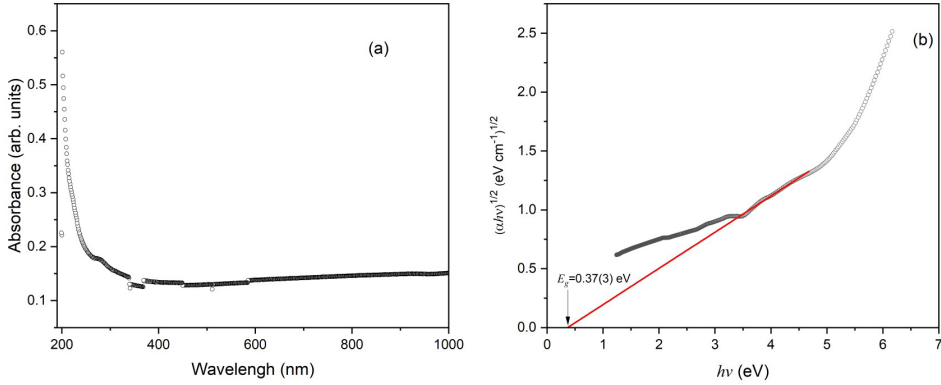


**Figure 5.** a) UV-Vis absorbance spectrum of the 25h milled sample and b) the corresponding Tauc plot (Equation 6) for the bandgap calculation.

The decrease of resistivity with the increase in temperature clearly indicates a semiconducting behavior. The resistivity at room-temperature (300 K) is approximately 1.05  $\Omega$ .mm. This value is consistent with the literature, i.e., Mohamed et al.<sup>8</sup> reported 1.2  $\Omega$ .mm at 323 K in a mechanically alloyed followed by spark plasma sintering sample; Young et al.<sup>12</sup> obtained 1.4  $\Omega$ .mm at 300 K in a NbFeSb alloy produced by arc-melting and annealing at 750  $^{\circ}$ C for 1 week; Tavassoli et al.<sup>2</sup> reported a value around 1.0  $\Omega$ .mm at 300 K for NbFeSb synthesized by conventional arc-melting and annealing.

### 3.3. UV-Vis

Figure 5a shows the UV-Vis absorbance spectra of the 25h milled sample recorded in the wavelength region of 200–1000 nm.

Wood and Tauc<sup>22</sup> proposed a method for determining the band gap using optical absorbance data plotted appropriately with respect to energy. The optical absorption depends on the difference between the photon energy and the band gap as follows<sup>36</sup>:

$$(\alpha hv)^{1/n} = C(hv - E_{gap}) \quad (6)$$

where,  $\alpha$  is the absorption coefficient,  $h$  is the Planck constant,  $\nu$  is the frequency,  $E_{gap}$  is the band gap and  $C$  is a

proportionality constant. The values of  $n$  for direct allowed, indirect allowed, direct forbidden, and indirect forbidden transitions are 1/2, 2, 3/2, and 3, respectively. As our DFT calculation (see section 3.4) predicts an indirect allowed transition, we thereby consider  $n=2$  in the above equation. Figure 5b shows the  $(\alpha hv)^{1/2}$  versus  $hv$  plot. Thus, the band gap energy ( $E_g$ ) obtained from the x-intercept of the line fitting the  $(\alpha hv)^{1/2} - hv$  plot, as indicated in Figure 5b, is 0.37(3) eV. An experimental value of 0.4 eV was obtained earlier by Hobbis et al.<sup>7</sup> for the NbFeSb sample prepared by induction melting of the elements.

In light of the experimental values of band gap and electrical resistivity obtained in this work, which are in good agreement with published values for *bulk* samples, we believe that the presence of secondary phases and the nanostructured features (multiple grain boundaries, nanometric crystallites size, defects) of our sample do not degrade the electrical and optical properties of the compound.

### 3.4. DFT calculations

There are several theoretical calculations on the electronic structure of NbFeSb compounds employing techniques based on DFT<sup>3,5,6,15,16,37-40</sup>. Most of the calculated values of bandgap fall within the range of 0.51 – 0.54 eV<sup>3,5,6,15,37,38,40</sup>. Figure 6 illustrates the band structures, total density of states

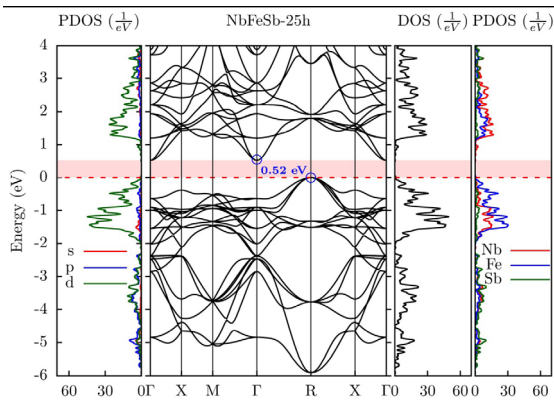


**Figure 6.** Calculated band structures, total density of states (DOS) and partial density of states (PDOS) for NbFeSb phase. The broad pink horizontal line represents the band gap.

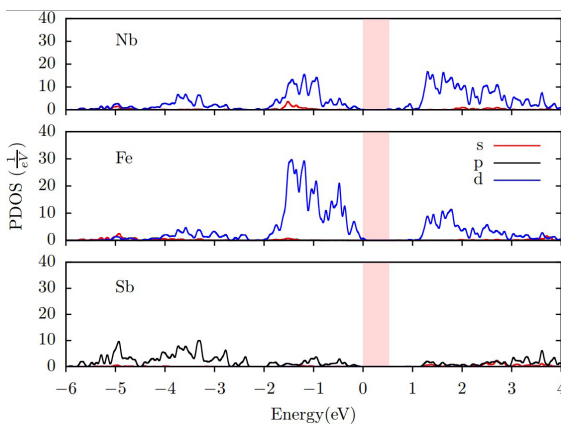


**Figure 7.** PDOS of the system illustrating the individual contribution of different atomic orbitals. The value of the highest occupied level of the valence band was taken as reference energy. The broad pink vertical line represents the gap region.

(DOS) and partial density of states (PDOS) for NbFeSb phase, obtained from our DFT calculations. The band structure shows that NbFeSb is semiconductor with an indirect bandgap of 0.52 eV between the high symmetry  $\Gamma$  and R points of the Brillouin zone. So, the present calculated bandgap is in excellent agreement with previous theoretical predictions, but slightly differs from that obtained experimentally (0.37 eV). Other HH compounds also present significant differences between experimental band gap values and band gap values calculated via DFT<sup>41-43</sup>. Depending on the synthesis method used to obtain the compound, the difference between the measured value of the gap and that obtained by simulation may increase.

Figure 7 presents the PDOS of the system illustrating the individual contribution of different atomic orbitals. As can be seen, the electrons of the d-orbitals dominate electronic transport process in NbFeSb. The valence band is predominantly contributed by Fe d-orbitals, while conduction band gets major contribution from Nb d-orbitals. Effective contribution of the Sb orbitals to DOS is negligible compared to Fe and Nb.

## 4. Conclusion

In this work, we have synthesized a nanostructured HH NbFeSb alloy directly by the simple and low cost process of mechanical alloying without any other type of processing. The structural parameters of NbFeSb alloy have been obtained from Rietveld refinement of the x-ray diffractogram. The average crystallite size of 9.54(2) nm and microstrain of 0.083% have been acquired from linear adjustment to Williamson-Hall equation. The DSC measurements have shown a wide exothermic curve with two main shoulders centered around 540 and 630 K. In situ high temperature XRD measurements in the range of 300 – 420 K have shown no changes in crystalline structure. These results indicate that the NbFeSb alloy produced by MA was stable only up to 420 K. As NbFeSb is a promising thermoelectric material for mid-to-high temperature applications (700 K – 1000 K), further investigation on thermal stability of NbFeSb produced only by MA is needed prior high temperature applications.

The CIS measurements have indicated that the sample has purely resistive behavior with an approximately constant resistance of 3.3  $\Omega$ . The behavior of the resistivity-temperature curve is similar to that of a semiconductor and the electrical resistivity at ambient temperature is about 1.05  $\Omega\text{mm}$ , which is in good agreement with others experimental results.

The band gap of 0.37(3) eV, obtained from UV-Vis absorbance spectra by a Tauc plot, is in fair agreement with other experimental results and DFT calculations.

As the electrical resistivity and band gap values obtained by us are in good agreement with those reported in literature for bulk NbFeSb, we may expect that the presence of secondary phases, structural defects and nanometric crystallites sizes of nanostructured NbFeSb produced by MA are able to decrease the thermal conductivity without degradation of electrical and optical properties of the compound, which is relevant for thermoelectric applications.

## 5. Acknowledgements

We acknowledge the financial support from the Brazilian funding agencies CAPES – Finance code 001, CNPq (grants 303809/2018-3 and 307655/2020-2) and FAPEAM (POSGRAD UFAM 2018, process 062.00478/2019). We thank the LabMat-UFAM, Nanopol-UFAM, LAMAC-UFAM and LMSC-UFAM laboratory facilities.

## 6. References

- Quinn RJ, Bos JWG. Advances in half-Heusler alloys for thermoelectric power generation. *Mater Adv.* 2021;2:6246-66. <http://dx.doi.org/10.1039/d1ma00707f>.
- Tavassoli A, Failamani F, Grytsiv A, Rogl G, Heinrich P, Müller H, et al. On the Half-Heusler compounds Nb<sub>1-x</sub>{Ti,Zr,Hf}<sub>x</sub>FeSb: phase relations, thermoelectric properties at low and high temperature, and mechanical properties. *Acta Mater.* 2017;135:263-76. <http://dx.doi.org/10.1016/j.actamat.2017.06.011>.
- Fang T, Zheng S, Chen H, Cheng H, Wang L, Zhang P. Electronic structure and thermoelectric properties of p-type half-Heusler compound NbFeSb: a first-principles study. *RSC Advances.* 2016;6:10507-12. <http://dx.doi.org/10.1039/c5ra23091h>.
- Joshi G, He R, Engber M, Samsonidze G, Pantha T, Dahal E, et al. NbFeSb-based p-type half-Heuslers for power generation

- applications. *Energy Environ Sci.* 2014;7:4070-6. <http://dx.doi.org/10.1039/c4ee02180k>.
5. Kumar N, Saini HS, Nisha, Singh M, Kashyap MK. Enhanced thermoelectric properties of hf doped half-heusler compound NbFeSb. *AIP Conf Proc.* 2020;2265:030459. <http://dx.doi.org/10.1063/5.0017704>.
  6. Kahi JN, Shenoy US, Kihoi SK, Kim H, Yi S, Bhat DK, et al. Optimized electronic performance in half-Heusler Ti-doped NbFeSb materials by stoichiometric tuning at the Fe and Sb sites. *J Alloys Compd.* 2022;891:162033. <http://dx.doi.org/10.1016/j.jallcom.2021.162033>.
  7. Hobbs D, Hermann RP, Wang H, Parker DS, Pandey T, Martin J, et al. Structural, chemical, electrical, and thermal properties of n-Type NbFeSb. *Inorg Chem.* 2019;58:1826-33. <http://dx.doi.org/10.1021/acs.inorgchem.8b02531>.
  8. Mohamed MAA, Ibrahim EMM, Rodriguez NP, Hampel S, Büchner B, Schiering G, et al. Tuning of the electronic and phononic properties of NbFeSb half-Heusler compound by Sn/Hf co-doping. *Acta Mater.* 2020;196:669-76. <http://dx.doi.org/10.1016/j.actamat.2020.07.028>.
  9. El-Khouly A, Adam AM, Altowairqi Y, Serhienko I, Chernyshova E, Ivanova A, et al. Transport and thermoelectric properties of Nb-doped FeV<sub>0.64</sub>Hf<sub>0.16</sub>Ti<sub>0.2</sub>Sb half-Heusler alloys synthesized by two ball milling regimes. *J Alloys Compd.* 2022;890:161838. <http://dx.doi.org/10.1016/j.jallcom.2021.161838>.
  10. El-Khouly A, Novitskii A, Serhienko I, Kalugina A, Sedegov A, Karpenkov D, et al. Optimizing the thermoelectric performance of FeV<sub>0.64</sub>Sb half-Heusler compound via Hf-Ti double doping. *J Power Sources.* 2020;477:228768. <http://dx.doi.org/10.1016/j.jpowsour.2020.228768>.
  11. Page A, Poudeu PFP, Uher C. A first-principles approach to half-Heusler thermoelectrics: accelerated prediction and understanding of material properties. *J Mater.* 2016;2:104-13. <http://dx.doi.org/10.1016/j.jmat.2016.04.006>.
  12. Young DP, Khalifah P, Cava RJ, Ramirez AP. Thermoelectric properties of pure and doped FeMSb (M=V,Nb). *J Appl Phys.* 2000;87:317-21. <http://dx.doi.org/10.1063/1.371863>.
  13. Shen J, Fan L, Hu C, Zhu T, Xin J, Fu T, et al. Enhanced thermoelectric performance in the n-type NbFeSb half-Heusler compound with heavy element Ir doping. *Mater Today Phys.* 2019;8:62-70. <http://dx.doi.org/10.1016/j.mtphys.2019.01.004>.
  14. Huang L, Zhang Q, Yuan B, Lai X, Yan X, Ren Z. Recent progress in half-Heusler thermoelectric materials. *Mater Res Bull.* 2016;76:107-12. <http://dx.doi.org/10.1016/j.matresbull.2015.11.032>.
  15. Zerrouki T, Rached H, Rached D, Caid M, Cheref O, Rabah M. First-principles calculations to investigate structural stabilities, mechanical and optoelectronic properties of NbCoSn and NbFeSb half-Heusler compounds. *Int J Quantum Chem.* 2021;121:1-12. <http://dx.doi.org/10.1002/qua.26582>.
  16. Naydenov GA, Hasnip PJ, Lazarov VK, Probert MIJ. Huge power factor in p-type half-Heusler alloys NbFeSb and TaFeSb. *Journal of Physics: Materials.* 2019;2(3):035002. <https://doi.org/10.1088/2515-7639/ab16fb>
  17. El-Khouly A, Novitskii A, Adam AM, Sedegov A, Kalugina A, Pankratova D, et al. Transport and thermoelectric properties of Hf-doped FeV<sub>0.64</sub>Sb half-Heusler alloys. *J Alloys Compd.* 2020;820:153413. <http://dx.doi.org/10.1016/j.jallcom.2019.153413>.
  18. El-Khouly A, Adam AM, Ibrahim EMM, Nafady A, Karpenkov D, Novitskii A, et al. Mechanical and thermoelectric properties of FeV<sub>0.64</sub>Sb-based half-Heusler alloys. *J Alloys Compd.* 2021;886:161308. <http://dx.doi.org/10.1016/j.jallcom.2021.161308>.
  19. El-Khouly A, Adam AM, Novitskii A, Ibrahim EMM, Serhienko I, Nafady A, et al. Effects of spark plasma sintering on enhancing the thermoelectric performance of Hf-Ti doped VFeSb half-Heusler alloys. *J Phys Chem Solids.* 2021;150:109848. <http://dx.doi.org/10.1016/j.jpcs.2020.109848>.
  20. Suryanarayana C. Mechanical alloying: a novel technique to synthesize advanced materials. *Research.* 2019;2019:1-17. <http://dx.doi.org/10.34133/2019/4219812>.
  21. Pedersen SV, Croteau JR, Kempf N, Zhang Y, Butt DP, Jaques BJ. Novel synthesis and processing effects on the figure of merit for NbCoSn, NbFeSb, and ZrNiSn based half-Heusler thermoelectrics. *J Solid State Chem.* 2020;285:121203. <http://dx.doi.org/10.1016/j.jssc.2020.121203>.
  22. Wood DL, Tauc J. Weak absorption tails in amorphous semiconductors. *Phys Rev B.* 1972;5:3144-51.
  23. Larson AC, Von Dreele RB, Alamos L. Laur 86-748 ©: General Structure Analysis System [Internet]. 2000 [cited 2022 June 26]. Available from <https://www.ems.psu.edu/~ryba/coursework/Advanced Powder Diffraction/GSASManual.pdf>
  24. Mccusker LB, Von Dreele RB, Cox DE, Louër D, Scardi P. Rietveld refinement guidelines. *J Appl Cryst.* 1999;32:36-50. <http://dx.doi.org/10.1107/S0021889898009856>.
  25. Pecharsky VK, Zavalij PY. Fundamentals of powder diffraction and structural characterization of materials. Boston, MA: Springer US; 2009. <https://doi.org/10.1007/978-0-387-09579-0>.
  26. Mittemeijer EJ, Welzel U. The “state of the art” of the diffraction analysis of crystallite size and lattice strain. *Zeitschrift Für Krist.* 2008;223:552-60. <http://dx.doi.org/10.1524/zkri.2008.1213>.
  27. Langford JJ, Wilson AJC. Scherrer after sixty years: a survey and some new results in the determination of crystallite size. *J Appl Cryst.* 1978;11:102-13. <http://dx.doi.org/10.1107/S0021889878012844>.
  28. Giannozzi P, Baroni N, Bonini N, Calandra M, Car R, Cavazzoni C, et al. QUANTUM ESPRESSO: a modular and open-source software project for quantum simulations of materials. *J Phys Condens Matter.* 2009;21. <http://dx.doi.org/10.1088/0953-8984/21/39/395502>.
  29. Perdew JP, Burke K, Ernzerhof M. Generalized gradient approximation made simple. *Phys Rev Lett.* 1996;77:3865-8. <http://dx.doi.org/10.1103/PhysRevLett.77.3865>.
  30. Pack JD, Monkhorst HJ. “Special points for Brillouin-zone integrations”: a reply. *Phys Rev B.* 1977;16:1748-9. <http://dx.doi.org/10.1103/PhysRevB.16.1748>.
  31. Kokalj A. Computer graphics and graphical user interfaces as tools in simulations of matter at the atomic scale. *Comput Mater Sci.* 2003;28:155-68. [http://dx.doi.org/10.1016/S0927-0256\(03\)00104-6](http://dx.doi.org/10.1016/S0927-0256(03)00104-6).
  32. Levin I. NIST Inorganic Crystal Structure Database (ICSD). Gaithersburg: National Institute of Standards and Technology; 2018. <https://doi.org/10.18434/M32147>.
  33. Toby BH. R factors in Rietveld analysis: how good is good enough? *Powder Diffr.* 2006;21:67-70. <http://dx.doi.org/10.1154/1.2179804>.
  34. Macdonald JR, Barsoukov E. Impedance spectroscopy: theory, experiment, and applications. 2nd ed. New Jersey: Wiley; 2018.
  35. Gao W, Li Z, Sammes N. An introduction to electronic materials for engineers, 2nd ed. Singapore: World Scientific; 2011. <https://doi.org/10.1142/7606>.
  36. Viezbicke BD, Patel S, Davis BE, Birnie DP. Evaluation of the Tauc method for optical absorption edge determination: ZnO thin films as a model system. *Phys Status Solidi Basic Res.* 2015;252:1700-10. <http://dx.doi.org/10.1002/pssb.201552007>.
  37. Yang J, Li H, Wu T, Zhang W, Chen L, Yang J. Evaluation of half-Heusler compounds as thermoelectric materials based on the calculated electrical transport properties. *Adv Funct Mater.* 2008;18:2880-8. <http://dx.doi.org/10.1002/adfm.200701369>.
  38. Fu C, Zhu T, Pei Y, Xie H, Wang H, Snyder GJ, et al. High band degeneracy contributes to high thermoelectric performance in p-type Half-Heusler compounds. *Adv Energy Mater.* 2014;4. <http://dx.doi.org/10.1002/aenm.201400600>.
  39. Çoban C, Çolakolu K, Çiftçi Y. First principles study of the structural, mechanical, phonon, optical, and thermodynamic

- properties of half-Heusler (HH) compound NbFeSb. *Phys Scr.* 2015;90. <http://dx.doi.org/10.1088/0031-8949/90/9/095701>.
40. Tian Y, Vagizov FG, Ghassemi N, Ren W, Zhu H, Wang Z, et al. Defect charging and resonant levels in half-Heusler Nb<sub>1-x</sub>Ti<sub>x</sub> FeSb. *Mater Today Phys.* 2021;16:100278. <http://dx.doi.org/10.1016/j.mtphys.2020.100278>.
41. Choudhary MK, Ravindran P. Thermal, electronic and thermoelectric properties of TiNiSn and TiCoSb based quaternary half Heusler alloys obtained from: ab initio calculations. *Sustain Energy Fuels.* 2020;4:895-910. <http://dx.doi.org/10.1039/c9se01047e>.
42. Birkel CS, Zeier WG, Douglas JE, Lettiere BR, Mills CE, Seward G, et al. Rapid microwave preparation of thermoelectric TiNiSn and TiCoSb half-Heusler compounds. *Chem Mater.* 2012;24:2558-65. <http://dx.doi.org/10.1021/cm3011343>.
43. Wang LL, Miao L, Wang ZY, Wei W, Xiong R, Liu HJ, et al. Thermoelectric performance of half-Heusler compounds TiNiSn and TiCoSb. *J Appl Phys.* 2009;105. <http://dx.doi.org/10.1063/1.3056384>.